Subcycle interference in high-order harmonic generation from solids

Tao-Yuan Du,[1,2] Dong Tang,[2,3] and Xue-Bin Bian[2,*]

[1]*School of Mathematics and Physics, China University of Geosciences, Wuhan 430074, China*

[2]*State Key Laboratory of Magnetic Resonance and Atomic and Molecular Physics, Wuhan Institute of Physics and Mathematics, Chinese Academy of Sciences, Wuhan 430071, China*

[3]*University of Chinese Academy of Sciences, Beijing 100049, China*

(Received 2 August 2018; published 14 December 2018)

Different from the high-order harmonic generation (HHG) from gases, we find that the yield of HHG from solids exhibits unexpected modulations as a function of the driving laser intensity and wavelength. Its mechanism can be unraveled by the interference between currents inside the solids induced by two adjacent Zener tunneling events. Our simulations agree well with the experimental measurements of HHG from ZnSe and solid Ar. We also find that the dephasing time plays a key role in this subcycle interference and can turn it on or off by controlling the overlap between the channels. It provides an avenue to optimize the ultrafast electron dynamics and HHG emission processes in solids, which will be useful for the compact ultrafast EUV light sources. We also propose an experimental scheme by using ultrashort lasers to explore this interference in other solid materials.

DOI: 10.1103/PhysRevA.98.063416

I. INTRODUCTION

High-order harmonic generation (HHG) has been studied extensively in atomic and molecular systems [1–3]. It can be well explained by the three-step recollision model. Recently, efficient HHG from solid materials has been attracting much attention [4–17]. It could give rise to more compact and brighter extreme ultraviolet light sources. This also provides us ultrafast tools to study the electron-hole dynamics in condensed-phase systems. Different physical mechanisms of HHG from solids have been proposed: only intraband transition [5,8], collective contributions from both intra and interband transitions [12–31], or generalized recollision of electrons and holes in the coordinate and momentum spaces [17–21].

The low conversion efficiency of HHG poses a significant and practical limitation for many applications. The intensity-dependent yield of HHG from gases is mainly determined by the ionization rate and the depletion of the bound state. When the depletion is negligible, the yield in the perturbative regime is proportional to I^q (I is the laser intensity, and q is the order). Then q gradually becomes small in the non-perturbative regime. In contrast, the yield will decrease ($q < 0$) when the laser field reaches the saturation threshold due to the strong depletion. For a constant laser intensity, the wavelength-dependent yield follows a $\lambda^{-(5-6)}$ scaling law [2,3] in the gas-phase HHG. For the wavelength scaling of crystal ZnO, a $\lambda^{-(11.4\pm2.9)}$ was measured [14]. The intensity-dependent yield of HHG from ZnO [22] is similar to that from gases. However, in Fig. 1, the HHG yield from ZnSe (data from Fig. 3(a) and Fig. S4 in Ref. [15]) and solid Ar (Fig. 2(a) in Ref. [10]) exhibits a strong modulation as a function of laser intensity, which is unexpected and not explained.

In this work, we develop an interference model to reveal the origin of the above-mentioned modulation and the reason for its absence in other materials.

II. THEORETICAL METHODS

The interaction between the laser fields and solid materials is simulated by solving the multiband semiconductor Bloch equations (SBEs), which can be also found in Refs. [16,17,23]. In the SBEs, the population and the polarization are written as

$$\dot{n}_m = i \sum_{m' \neq m} \Omega_{mm'} \pi_{mm'} e^{i S_{mm'}} + \text{c.c.}, \tag{1}$$

$$\dot{\pi}_{mm'} = -\frac{\pi_{mm'}}{T_2} + i \Omega^*_{mm'} (n_m - n_{m'}) e^{-i S_{mm'}} + i \sum_{m'' \notin \{m,m'\}} (\Omega_{m'm''} \pi_{mm''} e^{i S_{m'm''}} - \Omega^*_{mm''} \pi^*_{m'm''} e^{-i S_{mm''}}). \tag{2}$$

In Eqs. (1) and (2), we dropped the input (k, t) for simplicity. Here n_m is the population for band m and is subject to the constraint $\sum_m n_m = 1$. $S(k,t) = \int_{-\infty}^{t} \varepsilon_g(k,t')dt'$ is the classical action, ε_g is the band gap between the coupled energy bands $\Omega(k,t) = \mathbf{F}(t)\mathbf{d}(k,t)$ is the Rabi frequency. T_2 accounts for the dephasing time which phenomenologically describes the electron-phonon and electron-electron scattering processes. $\pi(k,t)$ is related to the interband polarization $\mathbf{P}(k,t) = \mathbf{d}(k,t)\pi(k,t)e^{iS(k,t)} + \text{c.c.}$ $\mathbf{d}(k)$ is the k-dependent transition dipole. We obtained $\mathbf{d}(k)$ and the band energies $E_m(k)$ by using the Vienna *ab initio* simulation package (VASP) code. The details in the calculations can be found in

*xuebin.bian@wipm.ac.cn

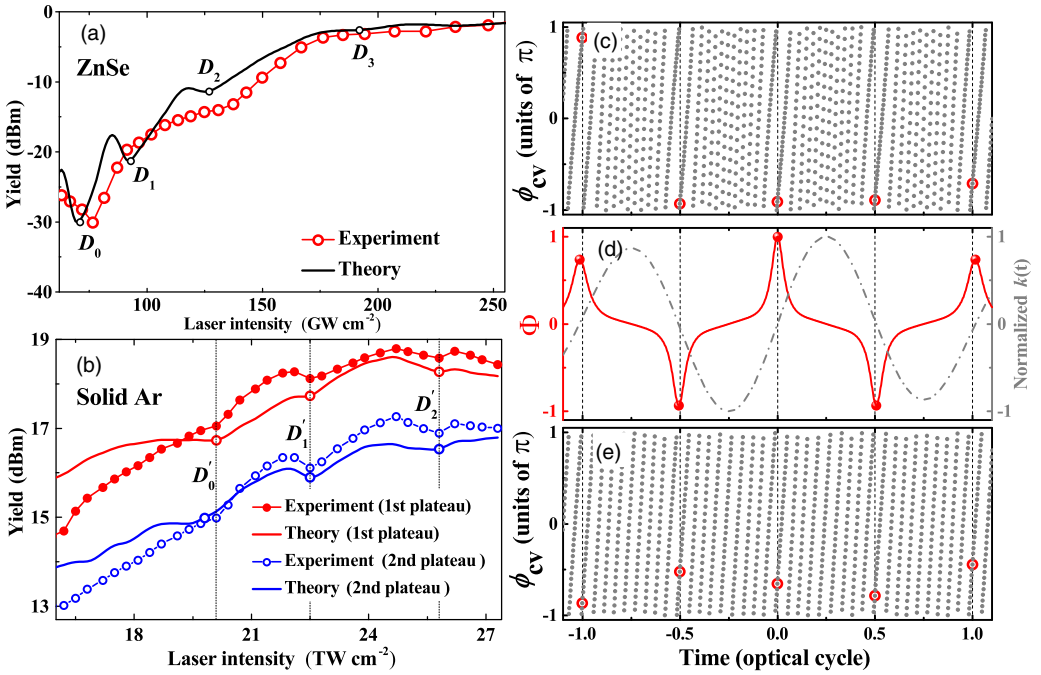

FIG. 1. (a) Comparison of the yield of the tenth harmonic in ZnSe as a function of laser intensity obtained from experimental measurements (redrawn from the experimental data in Fig. S4(f) of Ref. [15]) and our simulation of the SBEs. (b) Comparison of the integral yields of the first and second plateaus in solid Ar as a function of laser intensity obtained from the experimental data in Fig. 2(a) of Ref. [10] and our theoretical simulations. The yields of the first and second plateaus are integrated in the range of 19–25 and 25–33 eV, respectively. The minimal yield in the experimental data implies a destructive points, as denoted by $\boldsymbol{D}_{0,1,2,3}$ in (a) and $\boldsymbol{D}'_{0,1,2}$ in (b), respectively. Temporal evolutions of the propagation phase ϕ_{cv} at $\boldsymbol{D}_0$ and $\boldsymbol{D}'_0$ points are shown in (c) and (e), respectively. (d) Relative band coupling strength Φ, which is normalized and determines the times of the transition events. The transition events and its propagation phases are illustrated by the solid dots in (d) and hollow dot in (c) and (e), respectively. The dash-dotted line in (d) shows the electron wave vector $k(t)$.

Appendix A. The nonlinear currents by the laser-solid interaction are obtained by

$$\mathbf{j}_{\text{Intra}}(t) = \sum_m \int_{BZ} v_m(k) n_m(k,t) dk, \tag{3}$$

$$\mathbf{j}_{\text{Inter}}(t) = \frac{d}{dt} \int_{BZ} \mathbf{P}(k,t) dk, \tag{4}$$

where the band velocity v_m is defined by $\nabla_k E_m(k)$. The high harmonic spectrum is obtained from the Fourier transform (FT) of $\mathbf{j}_{\text{Total}} = \mathbf{j}_{\text{Intra}} + \mathbf{j}_{\text{Inter}}$, i.e.,

$$S_{\text{HHG}}(\omega) = |\widetilde{\mathbf{j}}_{\text{Total}}(\omega)|^2,$$

$$\widetilde{\mathbf{j}}_{\text{Total}}(\omega) = \frac{1}{\sqrt{2\pi}} \int_{-\infty}^{\infty} dt e^{-i\omega t} \mathbf{j}_{\text{Total}}(t). \tag{5}$$

The HHG yields of the plateau can be calculated by

$$Y = \int_{\omega_1}^{\omega_2} S_{\text{HHG}}(\omega) d\omega. \tag{6}$$

III. RESULTS AND DISCUSSIONS

We assume that the electric field **F**(t) of the laser pulse with a sine-squared envelope in the medium is linearly polarization along the Γ–K (L, M) direction for solid Ar(ZnSe,ZnO). Here the analysis is based on two bands for ZnSe and ZnO, i.e., the top valence ($m = v$) and the lowest conduction ($m = c$) band. Multibands have been involved for solid Ar to investigate the HHG in different plateaus. Figures 1(a) and 1(b) show the comparison of intensity-dependent HHG yields of ZnSe and

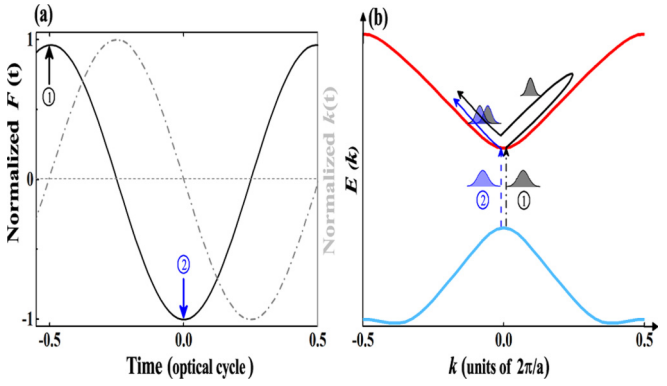

FIG. 2. Schematic of the subcycle interference. Two electron wave packets are pumped to the conduction band by Zener transition around the adjacent peaks which are separated by a half optical cycle. Temporal evolutions of the electron wave vector $k(t)$ is shown by the gray dash-dotted line in (a). The motion of wave packets in the same band shows the intraband current (solid arrows), while the ionization between valence and conduction bands illustrates the Zener transition (dashed arrows) in (b). The interference comes from the overlap between these two groups of the wave packets. $k = 0$ correspond to the Γ point in the reduced BZ.

solid Ar from experimental measurements in Refs. [10,15] and our SBEs simulations. The wavelength and the dephasing time are 5 μm, 20 fs for ZnSe and 1.333 μm, 10 fs for solid Ar, respectively. They agree quantitatively, especially the obvious minima at $I \approx 80$ and 140 GW/cm^2 for ZnSe and $I \approx 20$, 22, and 26 TW/cm^2 for solid Ar. One can surprisingly find that the positions of the minimal yield points in the first plateau of HHG from solid Ar agree well with the minima in the second plateau. This is not a coincidence. We will explain it next. The above modulation and the minima cannot be described by the Keldysh theory [32]. It should be attributed to some interference effect which is weak or absent in HHG from gases.

In Fig. 2, we propose a scheme for the subcycle interference within an optical cycle (o.c.) in the Brillouin zone (BZ). It can be described as follows: (1) the first Zener tunneling around $k = 0$; (2) electrons in the conduction band driven by the laser fields reach the maximal $k_{\max}$ (short trajectory) and come back to $k = 0$ (long trajectory) within a half cycle; (3) the second Zener transition event; (4) intraband currents which are contributed by the first and second transition events could interfere with each other, as shown in the overlap between two groups of wave packets. The transitions in (1) and (3) are Zener tunnel processes, which could lead to a π phase jump of the wave packet due to different signs of laser field $\mathbf{F}(t)$. On the other hand, the intraband motions of electron wave packet in (3) and (4) accumulate a propagation phase between the two transition events. The interference condition is determined by the total phase difference between the two groups of wave packets, which are pumped at the two adjacent transition events.

To gain closer insight, we define the temporal evolution of the interband transition probability which is determined by the ratio of the coupling between the two bands and energy gap between them. This ratio is given by $\Phi(t) \equiv \frac{\Omega(k,t)}{\varepsilon_g(k,t)}$, which is called the relative band coupling strength. A change in the sign of Φ means a difference of π in the transition phase of a single Zener event. The propagation phase is $\phi_{cv} \equiv \int_{t_1}^{t_2} \varepsilon_g(k, t')dt'$, where t_2 - $t_1 = \pi/\omega$ refers to the travel time between the two transition events occurred at the two adjacent peaks of $\Phi(t)$. The electron momentum in a given energy band follows the Bloch acceleration theorem [33], $(k, t) \equiv \mathbf{K}(t)$, which changes in time as $\mathbf{K}(t) = k - \int_{t_0}^{t} \mathbf{F}(t')dt'$, where $k = \mathbf{K}(t_0)$ is the initial momentum. The interference condition is determined by the total phase difference Θ between t_1 and t_2,

$$\Theta = \left\{ \frac{1 - \mathrm{sgn}\left[\frac{\Phi(t_2)}{\Phi(t_1)}\right]}{2}\pi \right\} + |\phi_{cv}(t_2) - \phi_{cv}(t_1)|, \qquad (7)$$

where the first and second terms denote the phase differences of transition and propagation, respectively.

Based on the above analysis, we analyze the temporal evolutions of the propagation phases ϕ_{cv} at the extreme points $\boldsymbol{D}_0$ in Fig. 1(a) and $\boldsymbol{D}_0'$ in Fig. 1(b), as shown in Figs. 1(c) and 1(e), respectively. In Fig. 1(d), we show the relative band coupling strength between conduction and valence bands. The transition events mainly occur at Γ point (see the analysis in Appendix B), which corresponds to the peaks of $\Phi(t)$, as shown by the solid dots. One can find that the propagation phase difference $\Delta\phi_{cv}$ between each two adjacent transition events satisfies $2n\pi$, plus a π-phase shift of the transition phase [i.e., change in signs of $\Phi(t)$ between t_1 and t_2], as shown in Figs. 1(c), 1(d), and 1(e). The destructive condition in Eq. (7) is satisfied at the extreme points $\boldsymbol{D}_0$ and $\boldsymbol{D}_0'$. We also checked the phase difference at $\boldsymbol{D}_{1,2,3}$ in Fig. 1(a) and $\boldsymbol{D}_{1,2}'$ in Fig. 1(b), they all satisfy the destructive condition and agree with the experimental measurements. The agreement of interference minima in the first and second plateaus in Fig. 1(b) is reasonable. The second plateau HHG comes from a step-by-step excitation from the first conduction band to the second conduction band, and then transits to the valence band [10,18,26]. As a result, the destructive intraband interference in the first conduction band will lead to the suppression of the HHG yield in the whole spectra.

HHG from ZnO has been experimentally studied by different groups [8,14,22]. However, it seems that the modulation is absent in the intensity-dependent yield. To further gain an insight into the mechanisms, we numerically simulate the corresponding SBEs.

Figure 3 shows the HHG yields as a function of the laser intensity. The dephasing time is 10 fs. In Fig. 3(a), the yields of below-gap harmonics as a function of the laser field intensity present clear harmonic peaks and absence of modulation. Conversely, a clear modulation in the harmonic yields and a relatively complex harmonic structure emerge in the plateau zone with the HHG energy in the range of 3.3–12 eV. To facilitate analysis, we make an integral of the harmonic intensities in the plateau zone and show the yields in Fig. 3(b). The extreme points in Fig. 3(a) predicted by Eq. (1) reach a good agreement with quantum simulations. Here we arbitrarily choose the destructive and constructive points in Fig. 3(b) denoted by the hollow triangles to study their phases. According to the timescale of a half optical cycle interval between each two transition events, one can approximatively separate out a series of the groups of transition events which are marked by three groups of dots, as shown in Figs. 3(c) and 3(d). Take the first group of transition events as an example, one can find a propagation phase difference $\Delta\phi_{cv} \approx 0$ between $t_1 = -1.5$ o.c. and $t_2 = -1$ o.c., and a transition phase π as illustrated in Figs. 3(c). Furthermore, other groups of the transition events, i.e., $[(t_1, t_2)] \equiv [(-0.5, 0), (0, 0.5), (1.0, 1.5)]$ o.c., hold a propagation phase difference $\Delta\phi_{cv} \approx 0$ or 2π and a π-phase shift of transition phase. They result in total phase differences $[\Theta \approx (2n + 1)\pi]$ which satisfy the destructive interference condition and minimum points of the HHG yield in Fig. 3(b) occur. On the other hand, the propagation phase difference is $\Delta\phi_{cv} \approx \pi$ between each two transition events in the above groups, as presented in Fig. 3(c). In addition to the transition phase π, they result in total phase differences $\Theta \approx 2n\pi$. That satisfies the condition of the constructive interference, and yield maxima appear in Fig. 3(b). Note that the transition events between the above-mentioned groups, i.e., $[(-1.0, -0.5), (0.5, 1.0)]$ o.c., hold a propagation phase difference $\Delta\phi_{cv} \approx \pi/2$ and do not meet the conditions of the subcycle interference, as illustrated in Figs. 3(c) and 3(b). They are attributed to the impact of the envelope of the laser pulses and are ignored here.

One could expect that the laser wavelengths also regulate the propagation phases between two adjacent transition events

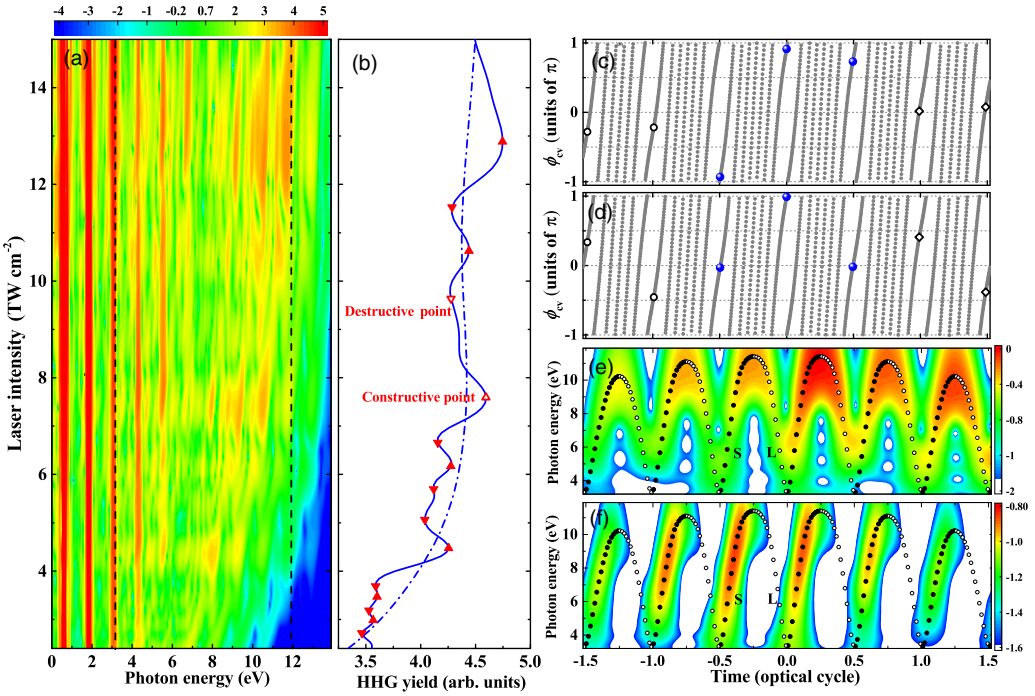

FIG. 3. Modulation of the HHG yields in ZnO crystal. (a) High harmonic spectra as a function of the laser intensity with constant laser frequency $\omega = 0.0228$ a.u., corresponding to a laser period $T_0 = 6.7$ fs. The duration is eight optical cycles. The dephasing time is $T_2 = 10$ fs. Two vertical dashed lines denote the minimal and maximal gap between the valence and conduction bands, which correspond to 3.3 and 12 eV, respectively. (b) Harmonic yields (blue solid line) which are the integrals of the plateau zone in the range of 3.3–12 eV as a function of the laser intensity. The destructive (downward triangle) and constructive (upward triangle) points of the HHG yield are predicted by the subcycle interference model. Two hollow triangles denote destructive and constructive points as an example, respectively. The role of dephasing time in modulation of HHG yields has been illustrated by the blue dash-dotted line in (b), where T_2 is about 3 fs in our simulations. Temporal evolutions of the propagation phase ϕ_{cv} at the destructive and constructive points of the HHG yield are shown in (c) and (d), respectively. Time-frequency analysis of HHG with $A_0 = 0.8\pi/a$ is presented with $T_2 = 10$ fs in (e) and $T_2 = 3$ fs in (f). The solid and hollow dots indicate the short (S) and long (L) trajectories, respectively, which are predicted by the quasiclassical model [18].

within a half optical cycle. In Fig. 4, we show the wavelength-dependent modulation of the HHG yield. One can find that the yield modulations are distinct. The interval of modulation is about 200 nm. The phase differences predict the emergence of

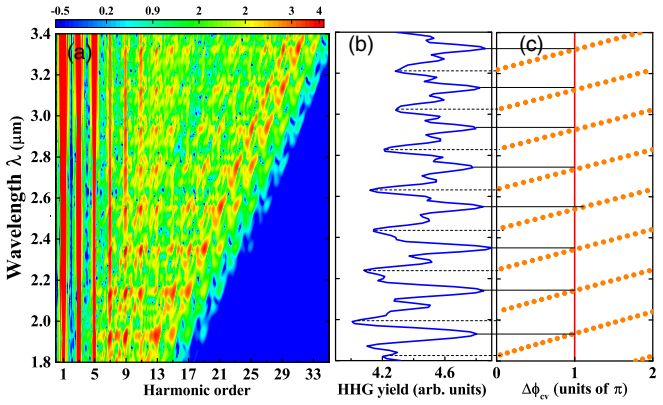

FIG. 4. (a) High harmonic spectra as a function of the wavelength λ with constant strength of the electric field $F_0 = 0.0079$ a.u. (b) Harmonic yields which are the integrals of the plateau zone as a function of the wavelength. (c) The propagation phase differences as function of the wavelength when the transition events occur at $t_1 = -0.5$ o.c. and $t_2 = 0$ o.c., respectively.

the constructive and destructive points well which are denoted by horizontal solid and dashed lines, respectively.

So far our simulations deviate from the experimental measurements of ZnO in which the HHG yield modulation is absent [8,22]. From the above analysis, the yield modulation is from the subcycle interference between two adjacent transition events, as shown in Fig. 2. The possible reason may come from the dephasing time. When the timescale of electron-electron or electron-phonon scattering is comparable to a half of an optical cycle, the long trajectories of electrons could be weakened [16]. It can turn off the overlap between the two wave packets in Fig. 2 and should lead to the absence of the modulation of the yields of the HHG in the plateau zone.

Let us make a control of electron trajectories by changing the dephasing time from 10 to 3 fs. One can find a smooth increase of the HHG yields, as illustrated by blue dash-dotted line in Fig. 3(b). It reaches a good agreement with the experimental results [8,22]. The scaling parameter q of intensity-dependent yield is bigger under the low intensity (multiphoton limit), but is smaller for a high intensity (tunneling regime). To assess the role of the dephasing time in the subcycle interference, we show the time-frequency analyses [34] of HHGs with $T_2 = 10$ fs and 3 fs in Figs. 3(e) and 3(f), respectively. One can find that the emission times by the quantum simulations and quasiclassical predictions [18] show a good agreement with each other. The damping of the long

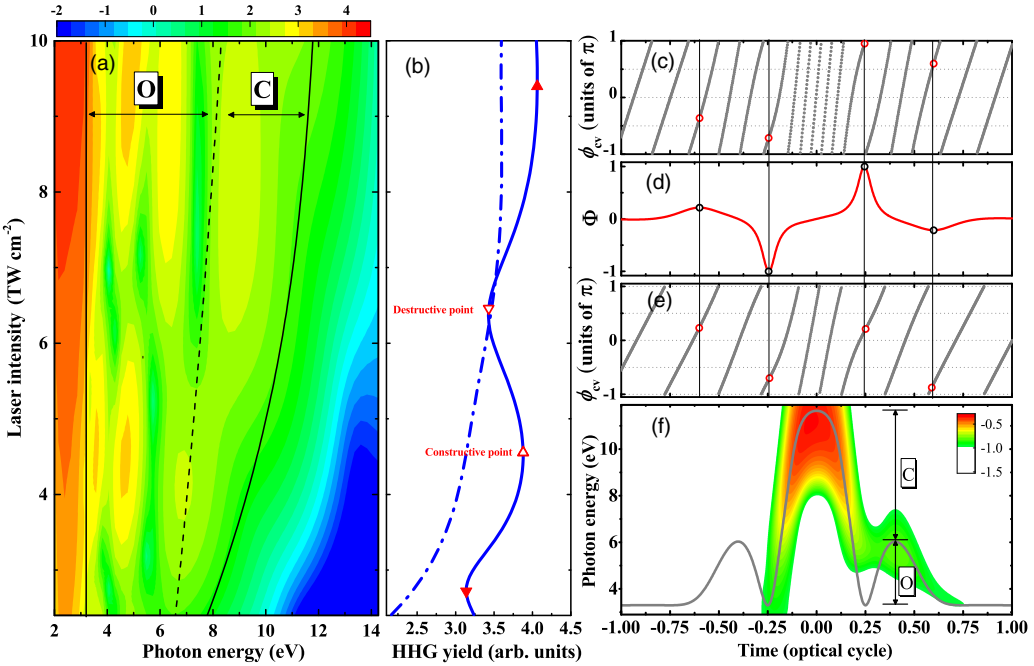

FIG. 5. Demonstration of the subcycle interference in a single-cycle laser pulse. (a) HHG spectra as a function of the laser intensity. The laser frequency $\omega = 0.0351$ a.u., corresponding to a period about 4.3 fs. The FWHM of the laser pulse is about one cycle. HHGs in the plateau zone are divided into two zones which correspond to the interference opening (**O**) and closing (**C**) channels. (b) The harmonic yields which are the integrals of the zones in the HHG range of the interference opening (solid line) and closing (dash-dotted line) as a function of the laser intensity. The extreme points of the HHG yield in the interference opening zone are predicted by the above model, as shown by the downward and upward triangles in (b). Temporal evolution of the propagation phase ϕ_{cv} at the destructive and constructive points of the HHG yield [two hollow triangles in (b)] are shown in (c) and (e), respectively. (d) Band coupling strength Φ. The hollow dots in (c), (d), and (e) denote the transition events. (f) Time-frequency profile and quasiclassical prediction of HHG emission in (a) where the laser intensity is 9.67 TW/cm^2.

trajectories is obvious in Fig. 3(f) compared to Fig. 3(e). That gives rise to the suppression of the temporal overlap between two adjacent transition events, and the interference between them is consequently negligible.

Generally, the dephasing time in the solid-state materials is determined by complex mechanisms, such as electron-electron correlations, dopant, temperature, and light-induced gap [35–38]. Although it is very difficult to precisely regulate the dephasing time experimentally, we can control the optical period and the pulse duration of the driving laser, suppress the dephasing effect, and further control the number of transition events to identify the subcycle interference effect.

The damage threshold for short-wavelength lasers may be lower, but the very short pulse duration will compensate it. In Fig. 5, we demonstrate the HHG in ZnO driven by the single-cycle laser pulses [39,40] with wavelength 1.3 μm. The dephasing time $T_2 = 3$ fs has been adopted in our calculations. Electrons which are excited at the low and high peaks of the coupling strength Φ, respectively, can be classified into two groups, as shown by dots in Fig. 5(d). These two groups of electrons have a mapping range difference in the BZ, as shown in Fig. 5(f). This dynamic range difference determines the boundary between the interference opening (**O**) and nearly closing (**C**) zones, which are shown in Figs. 5(a) and 5(f). Since one group of the electrons are confined to the lower wave-vector zone, the approximative interference closing can be attributed to the absence of the interference in the higher wave-vector zone between these two groups of electrons.

One can distinguish the interference opening and closing zones in Figs. 5(a) and 5(b). The oscillation (solid line) and smooth increase (dash-dotted line) of the HHG yields prove that the interference is turned on and of,f respectively, by the waveform of the laser pulse. The extreme points predicted by Eq. (7) also show a good agreement with the quantum simulations. Two representative points are marked by hollow triangles in Fig. 5(b). In Figs. 5(c) and 5(e), temporal evolutions of the propagation phase ϕ_{cv} provide an insight to understand the emergence of the destructive and constructive points in Fig. 5(b), respectively. The interference mechanisms are the same as those in Figs. 1 and 3.

IV. CONCLUSION

In conclusion, the unexpected yield modulations of HHG from ZnSe and solid Ar are studied numerically. This effect is due to the quantum interference between two paths, which are induced by two adjacent transition events. It is not considered in previous theories, but of significant importance since the interference may lead to 20% enhancement or suppression in HHG yield. After taking the role of higher conduction bands into consideration by the step-by-step model [18,21], it can explain well that the modulations of HHG from Ar in the first and second plateaus are quite similar. The dephasing time can turn the interference effect on and off and then regulate the emergence of modulation in the HHG yields. We also study the possible experimental realization scheme in other

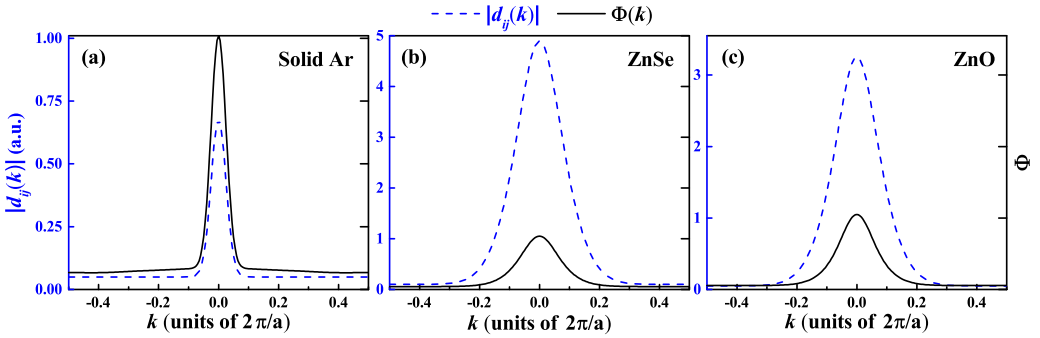

FIG. 6. The k-dependent values of the transition dipoles $|\mathbf{d}_{ij}(k)|$ (blue dashed lines) and relative band coupling strengths $\Phi(k)$ (black solid lines) between the valence (V) and the conduction (C1) bands along the directions of the corresponding optical axes. The relative band coupling strengths $\Phi(k)$ are normalized.

solid materials. The interference effect should be observed experimentally in the HHG spectra from solid-state materials driven by the ultrashort high-frequency lasers [38], even though the dephasing time of the material is very short. This subcycle interference will also affect the electron emission from nanotips [41].

ACKNOWLEDGMENTS

The authors thank H.-H. Yang, T.-J. Shao, and M. Huang for helpful discussions. This work is supported by the National Natural Science Foundation of China (NSFC) (Grants No. 91850121 and No. 11674363).

T.-Y.D. and D.T. contributed equally to this work.

APPENDIX A: ENERGY BANDS AND k-DEPENDENT DIPOLE ELEMENTS

Before the simulations of the light-solid interaction are performed, accurate band structure and transition dipole moments are required. We obtain these quantities via the density functional theory with a plane-wave basis set, using the Vienna *ab initio* simulation package (VASP) code [42,43]. The equilibrium structure calculations of the crystal materials are performed within the generalized gradient approximation (GGA) in the form of the Perdew and Wang (PW91) functional which is used to approximate exchange and correlation potentials. The cutoff energy of 550 eV is employed for the plane-wave basis expansion. The convergence criteria for the total energies and ionic forces are set to be 10^{-8} eV and 10^{-5} eVÅ^{-1} in the formula unit. By using the the Rayleigh-Schrödinger perturbation theory, the k-dependent transition dipole moments are related to the momentum elements $\hat{p}_{mm'}(k)$ as

$$\mathbf{d}_{m'm}(k) = i \cdot \frac{\hat{p}_{m'm}}{E_{m'}(k) - E_m(k)},$$
$$\hat{p}_{m'm}(k) = \langle u_{m',k}(r)|\hat{p}|u_{m,k}(r)\rangle,$$

where $|u_{m,k}(r)\rangle$ is the periodic part of the Bloch function in band index m with crystal momentum k. Once the Bloch function is calculated, the value of the transition dipole elements can also be calculated.

The calculated energy bands are fitted with the function $E_m(k) = \sum_{i=0}^{\infty} \alpha_{m,i} \cos(ika)$. The coefficients are listed in Table I. The orientations of the reciprocal lattices of solid materials are chosen for solid Ar $\parallel \Gamma K$, ZnSe $\parallel \Gamma L$, and ZnO $\parallel \Gamma M$, respectively. a is the lattice constant along the corresponding directions (optical axes) which are set as 7.78, 12.56 and 5.32 a.u., respectively.

In Fig. 6, the transition dipole $|\mathbf{d}_{ij}(k)|$ and relative band coupling strength $\Phi(k)$ are presented. The transition dipoles show a good agreement with the results in Refs. [44–48].

APPENDIX B: ROLE OF THE INITIAL K AROUND Γ POINT IN THE TRANSITION EVENTS

Field-induced photocarrier generation in an off-resonant regime is well described by Keldysh theory. For the laser intensities used in this work, carrier generations mainly occur in the part of the BZ where the corresponding transition dipole is maximal. Due to the exponential decay of the relative band coupling strengths $\Phi(k)$, as shown in Fig. 6, which lead to the small transition probability for k beyond $0.1k_{\max}$, we

TABLE I. Coefficients of the expansion of the energy bands.

Solid Ar	V	C1	C2
α_0	−0.1095	16.1063	20.4785
α_1	0.1416	−2.1027	1.4533
α_2	−0.0412	−0.0469	0.1529
α_3	0.0156	0.0941	0.1929
α_4	−0.0109	0.1293	0.0517
α_5	0.0072	0.1112	−0.0681
ZnSe			
α_0	−0.0919	0.1412	
α_1	0.0821	−0.0199	
α_2	0.0101	−0.0121	
α_3	0.0026	−0.0032	
α_4	0.0011	−0.0007	
α_5	0.0005	−0.0005	
ZnO			
α_0	−0.0928	0.2111	
α_1	0.0705	−0.0814	
α_2	0.0200	−0.0024	
α_3	−0.0012	−0.0048	
α_4	0.0029	−0.0003	
α_5	0.0006	−0.0009	

can safely conclude that the modulations of the HHG yields are determined by the transition events which mainly occur around Γ point. For transitions from the valence band to the lowest conduction band, as an example of ZnO, $\mathbf{d}(k)$ are maximal at the Γ point ($k_0 = 0$) and sharply decrease for $|k_1| \gtrsim \Delta k = 0.1k_{\max}$, as shown in Fig. 6(c). Let us make an estimation of the possibility that the modulations of the HHG yields are induced by the interference between two electron wave packets with the different initial momenta $\pm k_1$. Its condition is governed by the $\Delta\phi_{cv} = \Phi(k_1)\int_0^\tau \varepsilon_g(k_1, t')dt' \lesssim \pi/2$ and transition phase 0 in Eq. (7) (electron wave packets with momenta $\pm k_1$ are excited synchronously at the same peaks of the laser fields), where $\tau \sim 2\Delta k/\mathbf{F}_0$ is the propagating time delay between two wave packets. It gives rise to a small phase difference Θ and can be neglected in this work. In one word, the conclusion that the quantum interference between the transition events which occur mainly at Γ point leads to the modulation of the HHG yields can be supported convincingly.

[1] F. Krausz and M. Ivanov, Rev. Mod. Phys. **81**, 163 (2009).
[2] J. Tate, T. Auguste, H. G. Muller, P. Salieres, P. Agostini, and L. F. DiMauro, Phys. Rev. Lett. **98**, 013901 (2007).
[3] A. D. Shiner, C. Trallero-Herrero, N. Kajumba, H. C. Bandulet, D. Comtois, F. Legare, M. Giguere, J. C. Kieffer, P. B. Corkum, and D. M. Villeneuve, Phys. Rev. Lett. **103**, 073902 (2009).
[4] F. H. M. Faisal and J. Z. Kamiński, Phys. Rev. A **56**, 748 (1997).
[5] K. A. Pronin and A. D. Bandrauk, Phys. Rev. Lett. **97**, 020602 (2006).
[6] M. Ciappina, J. A. Pérez-Hernández, T. Shaaran, and M. Lewenstein, Eur. Phys. J. D **68**, 172 (2014).
[7] K. K. Hansen, D. Bauer, and L. B. Madsen, Phys. Rev. A **97**, 043424 (2018).
[8] S. Ghimire, A. D. DiChiara, E. Sistrunk, P. Agostini, L. F. DiMauro, and D. A. Reis, Nat. Phys. **7**, 138 (2011).
[9] S. Y. Kruchinin, F. Krausz, and V. S. Yakovlev, Rev. Mod. Phys. **90**, 021002 (2018).
[10] G. Ndabashimiye *et al.*, Nature **534**, 520 (2016).
[11] T. T. Luu *et al.*, Nature **521**, 498 (2015).
[12] M. Hohenleutner *et al.*, Nature **523**, 572 (2015).
[13] O. Schubert *et al.*, Nat. Photonics **8**, 119 (2014).
[14] Z. Wang *et al.*, Nat. Commun. **8**, 1686 (2017).
[15] A. A. Lanin *et al.*, Optica **4**, 516 (2017).
[16] G. Vampa and T. Brabec, J. Phys. B **50**, 083001 (2017).
[17] G. Vampa, C. R. McDonald, G. Orlando, D. D. Klug, P. B. Corkum, and T. Brabec, Phys. Rev. Lett. **113**, 073901 (2014).
[18] T.-Y. Du and X.-B. Bian, Opt. Express **25**, 151 (2017).
[19] N. Tancogne-Dejean *et al.*, Nat. Commun. **8**, 745 (2017).
[20] T.-Y. Du, X.-H. Huang, and X.-B. Bian, Phys. Rev. A **97**, 013403 (2018).
[21] G.-R. Jia, X.-H. Huang, and X.-B. Bian, Opt. Express **25**, 23654 (2017).
[22] S. Ghimire, A. D. DiChiara, E. Sistrunk, U. B. Szafruga, P. Agostini, L. F. DiMauro, and D. A. Reis, Phys. Rev. Lett. **107**, 167407 (2011).
[23] T.-Y. Du, D. Tang, X.-H. Huang, and X.-B. Bian, Phys. Rev. A **97**, 043413 (2018).
[24] M. Wu, S. Ghimire, D. A. Reis, K. J. Schafer, and M. B. Gaarde, Phys. Rev. A **91**, 043839 (2015).
[25] P. G. Hawkins, M. Y. Ivanov, and V. S. Yakovlev, Phys. Rev. A **91**, 013405 (2015).
[26] T. Ikemachi, Y. Shinohara, T. Sato, J. Yumoto, M. Kuwata-Gonokami, and K. L. Ishikawa, Phys. Rev. A **95**, 043416 (2017).
[27] S. Jiang, H. Wei, J. Chen, C. Yu, R. Lu, and C. D. Lin, Phys. Rev. A **96**, 053850 (2017).
[28] K. K. Hansen, T. Deffge, and D. Bauer, Phys. Rev. A **96**, 053418 (2017).
[29] J. Z. Jin, X. R. Xiao, H. Liang, M. X. Wang, S. G. Chen, Q. Gong, and L. Y. Peng, Phys. Rev. A **97**, 043420 (2018).
[30] L. Liu, J. Zhao, W. Dong, J. Liu, Y. Huang, and Z. Zhao, Phys. Rev. A **96**, 053403 (2017).
[31] X. Liu, X. Zhu, P. Lan, X. Zhang, D. Wang, Q. Zhang, and P. Lu, Phys. Rev. A **95**, 063419 (2017).
[32] L. Keldysh, JETP **20**, 1307 (1965).
[33] F. Bloch, Z. Phys. A **52**, 555 (1929).
[34] C. Chandre, S. Wiggins, and T. Uzer, Physica D **181**, 171 (2003).
[35] R. E. F. Silva, I. V. Blinov, A. N. Rubtsov, O. Smirnova, and M. Ivanov, Nat. Photonics **12**, 266 (2018).
[36] M. D. Webb, S. T. Cundiff, and D. G. Steel, Phys. Rev. B **43**, 12658 (1991).
[37] Q. T. Vu, H. Haug, O. D. Mucke, T. Tritschler, M. Wegener, G. Khitrova, and H. M. Gibbs, Phys. Rev. Lett. **92**, 217403 (2004).
[38] H. Mashiko *et al.*, Nat. Commun. **9**, 1468 (2018).
[39] Y. Kawakami *et al.*, Phys. Rev. B **95**, 201105(R) (2017).
[40] Y. Kawakami *et al.*, Nat. Photonics **12**, 474 (2018).
[41] J. Schötz *et al.*, Phys. Rev. A **97**, 013413 (2018).
[42] G. Kresse and J. Furthmüller, Phys. Rev. B **54**, 11169 (1996).
[43] J. P. Perdew, K. Burke, and M. Ernzerhof, Phys. Rev. Lett. **77**, 3865 (1996).
[44] R. S. Knox and F. Bassani, Phys. Rev. **124**, 652 (1961).
[45] L. F. Mattheiss, Phys. Rev. **133**, A1399 (1964).
[46] E. Ghahramani, D. J. Moss, and J. E. Sipe, Phys. Rev. B **43**, 9700 (1991).
[47] M. Goano, F. Bertazzi, M. Penna, and E. Bellotti, J. Appl. Phys. **102**, 083709 (2007).
[48] C. R. McDonald, G. Vampa, P. B. Corkum, and T. Brabec, Phys. Rev. A **92**, 033845 (2015).